Ultra-wideband RCS reduction using novel configured chessboard metasurface*

Ya-Qiang Zhuang(庄亚强), Guang-Ming Wang(王光明)†, and He-Xiu Xu(许河秀)

Air and Missile Defense College, Air Force Engineering University, Xi'an 710051, *China*

(Received 21 September 2016; revised manuscript received 17 November 2016; published online 30 March 2017)

A novel artificial magnetic conductor (AMC) metasurface is proposed with ultra-wideband 180° phase difference for radar cross section (RCS) reduction. It is composed of two dual-resonant AMC cells, which enable a broadband phase difference of 180°±30° from 7.9 GHz to 19.2 GHz to be achieved. A novel strategy is devised by dividing each rectangular grid in a chessboard configuration into four triangular grids, leading to a further reduction of peak bistatic RCS. Both full-wave simulation and measurement results show that the proposed metasurface presents a good RCS reduction property over an ultra-wideband frequency range.

Keywords: radar cross section reduction, artificial magnetic conductor, ultra-wideband, metasurface

PACS: 41.20.Jb, 42.25.Bs, 78.20.Ci **DOI:** 10.1088/1674-1056/26/5/054101

1. Introduction

With the pressing demand of stealth platforms, reducing the electromagnetic (EM) backscatter from metallic objectives attracts a great deal of attention. Generally speaking, two methods for radar cross section (RCS) reduction are commonly available: changing the object structure to redirect the scattered waves away from the incidence direction and loading radar absorbing material (RAM) on the object.[1,2] However, both methods somewhat suffer from complex design, bulky volume, and narrow operation bandwidth.

It is highly desirable to develop a thin surface for RCS reduction over a wide frequency range. Low-reflection metasurfaces have been adopted to overcome the aforementioned drawbacks. Several methods have been used to reduce the backscatter, such as using metamaterial absorbers,[3,4] random phase metasurface,[5–7] phase gradient metasurface (PGM),[8,9] and artificial magnetic conductor (AMC) chessboard surfaces.[10–14] In Ref. [5], the hybrid optimization algorithm was adopted to broaden the bandwidth for RCS reduction. A three-layer stacked patch was also employed to engineer broadband RCS reduction.[7] PGM enables high-efficiency propagating-wave to surface-wave conversion, deflected reflection, or diffused reflection if appropriately designed. By taking advantage of these merits, wideband RCS reduction was achieved by using PGM.[8] In comparison with shaping technology, the effect of a chessboard surface is similar to shaping technology, and the design of the chessboard configuration is easier. Thus, the chessboard surface is another essential technique for RCS reduction. Within the operation frequency of an AMC, the AMC tiles perform an in-phase reflection while the PEC tiles reflect the wave by 180° change which is cancelled by the AMC tiles. Hence, the reflect wave is redirected away from the incidence direction, leading to the reduction of backscatter RCS.[10] Since the AMC is an electromagnetic band-gap (EBG) structure with a narrow-band in-phase reflection,[15] the PEC tiles have been substituted by other AMC tiles to enhance the bandwidth of 180° phase difference.[11–14]

In this paper, we propose a metasurface design to achieve ultra-wideband and wide-angle RCS reduction. A novel configured chessboard metasurface is proposed by increasing the number of interfaces between adjacent AMC tiles, redirecting the incident wave into eight reflected lobes. As a result, the bistatic RCS is further attenuated. Two dual-mode AMC cells are cautiously designed to achieve an ultra-wideband RCS reduction. Simulations and measurement results show that the 10 dB RCS reduction bandwidth is over 70%. In addition, the performance for oblique angle of incidence up to 40° is examined.

2. Fundamentals and design

2.1. Theoretical analysis

The working mechanism of the chessboard AMC metasurface for RCS reduction is that the backscattered field will cancel and form different scattering lobes when the phase difference of the reflected fields between the two kinds of AMC tiles is 180°. The conventional chessboard metasurface as shown in Fig. 1(a) can be regard as a rectangular array consisting of two kinds of AMC tiles which have a phase difference of 180°. So the scattered field can be quantitative analyzed by the planar array theory.[12] Figure 1(b) depicts the proposed novel configured chessboard by dividing each rectangular grid

*Project supported by the National Natural Science Foundation of China (Grant Nos. 61372034 and 61501499).

†Corresponding author. E-mail: wgming01@sina.com

© 2017 Chinese Physical Society and IOP Publishing Ltd

into four triangular grids. The new topology significantly increases the number of interfaces between two kinds of AMC. Similarly, the scattered field of this novel configuration can also be analyzed by the planar array theory after some approximate equivalent.

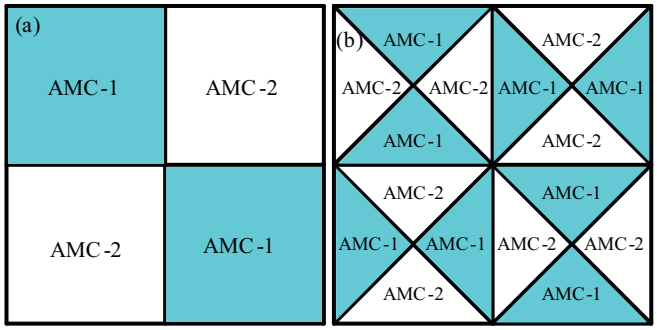


Fig. 1. (color online) Configurations of (a) conventional chessboard and (b) novel configured chessboard.

In the spherical system defined by elevation angle θ and azimuth angle φ, we suppose that the array factor of the (m, n)-th element is represented by

$$f_{mn}(\theta,\varphi) = \mathrm{e}^{\mathrm{j}m\psi_x}\,\mathrm{e}^{\mathrm{j}n\psi_y}\,\mathrm{e}^{\mathrm{j}\varphi_{mn}}, \tag{1}$$

where $\psi_x = k\Delta x\sin\theta\cos\varphi$, $\psi_y = k\Delta y\sin\theta\sin\varphi$, φ_{mn} is the phase of the (m,n)-th element, $k = 2\pi/\lambda$ is the wave number in free space, and Δx and Δy are the spacings between the tiles along the x-axis and y-axis, respectively. Therefore, the total array factor of a planar array can be written as

$$f_{\text{total}} = \sum_{m=0}^{M-1}\sum_{n=0}^{N-1} f_{mn}(\theta,\varphi) = \sum_{m=0}^{M-1}\sum_{n=0}^{N-1} \mathrm{e}^{\mathrm{j}m\psi_x}\,\mathrm{e}^{\mathrm{j}n\psi_y}\,\mathrm{e}^{\mathrm{j}\varphi_{mn}}, \tag{2}$$

where M and N are the numbers of elements along the x and y directions, respectively. Due to 180° phase difference between adjacent elements, $\mathrm{e}^{\mathrm{j}\varphi_{mn}}$ of each element is calculated as either 1 or -1. We assume that the AMC-1 tiles are represented by "1" items, while the AMC-2 tiles are represented by "-1" items. Therefore, for the conventional chessboard configuration with 4×4 tiles, the distribution of $\mathrm{e}^{\mathrm{j}\varphi_{mn}}$ can be expressed as

$$\mathrm{e}^{\mathrm{j}\varphi_{mn}} = \begin{bmatrix} 1 & -1 & 1 & -1 \\ -1 & 1 & -1 & 1 \\ 1 & -1 & 1 & -1 \\ -1 & 1 & -1 & 1 \end{bmatrix}. \tag{3}$$

Because the proposed novel configuration is not a rectangular mesh, it cannot be represented by a phase matrix directly. We divide a tile of novel configuration into nine equal-area square meshes, as shown in Fig. 2. Consequently, the usage of the phase matrix for the novel configuration is similar to the aforementioned. In addition, "0" items are adopted to represent the meshes comprised of both AMC-1 and AMC-2, which do not contribute to the scattered fields in the theoretical analysis.

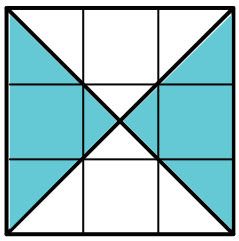


Fig. 2. (color online) The schematic of approximate equivalent method.

For the proposed configuration with 2×2 tiles shown in Fig. 1(b), the distribution of $\mathrm{e}^{\mathrm{j}\varphi_{mn}}$ can be expressed as

$$\mathrm{e}^{\mathrm{j}\varphi_{mn}} = \begin{bmatrix} 0 & 1 & 0 & 0 & -1 & 0 \\ -1 & 0 & -1 & 1 & 0 & 1 \\ 0 & 1 & 0 & 0 & -1 & 0 \\ 0 & -1 & 0 & 0 & 1 & 0 \\ 1 & 0 & 1 & -1 & 0 & -1 \\ 0 & -1 & 0 & 0 & 1 & 0 \end{bmatrix}. \tag{4}$$

By substituting Eqs. (3) and (4) into Eq. (2), the three-dimensional (3D) scattered fields for both configurations with the same dimensions can be theoretically calculated with the aid of software Matlab, see Fig. 3. As is shown, four main scattered lobes symmetrically position along the diagonal direction for the conventional chessboard structure. However for the novel topology, the number of scattered lobes is increased to eight, which would result in a lower peak bistatic RCS value.

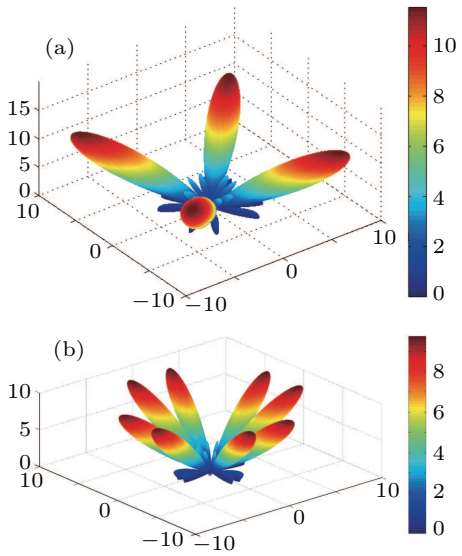


Fig. 3. (color online) Theoretical 3D scattered fields of (a) conventional chessboard and (b) novel configured chessboard.

2.2. Unit cell and metasurface design

In terms of the criterion set in the previous section, we designed two kinds of AMC cells, as shown in Fig. 4. As is shown, both AMCs have a sandwich-like structure, namely, a top metallic structure, a middle FR4 substrate with a thickness of 3 mm and a dielectric constant of 2.65, and a bottom metallic ground. The metallic composite of the first AMC (Fig. 4(a))

is composed of a cross and cross loop, whereas that of the second AMC (Fig. 4(b)) is a cross loaded terminal end with a C-shaped structure. For analysis convenience, these two elements are termed as AMC-1 and AMC-2, respectively. In the simulation setup shown in Fig. 4(c), the unit-cell boundary condition is assigned along x- and y-directions, and the open boundary condition is applied for the z-direction. For broadband RCS reduction, the geometrical parameters were cautiously designed with an optimum bandwidth of 180° phase difference. For this purpose, each AMC was independently characterized in CST microwave studio to obtain the reflection coefficients response. The optimum dimensions of the two AMCs are $p = 6$ mm, $w = 1.52$ mm, $a = 0.6$ mm, $b = 0.2$ mm, $l_1 = 3.2$ mm, $l_2 = 5.48$ mm, $l_3 = 1.5$ mm, $c = 0.3$ mm, and $d = 0.52$ mm.

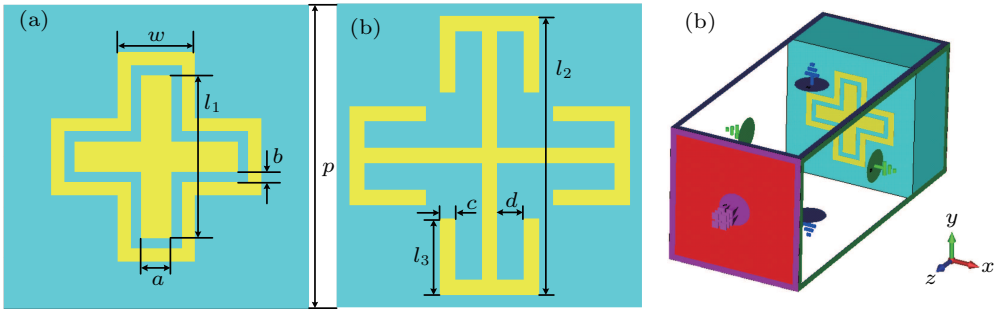


Fig. 4. (color online) Topology and simulation setup of utilized AMC unit cells: (a) AMC-1, (b) AMC-2, (c) simulation setup.

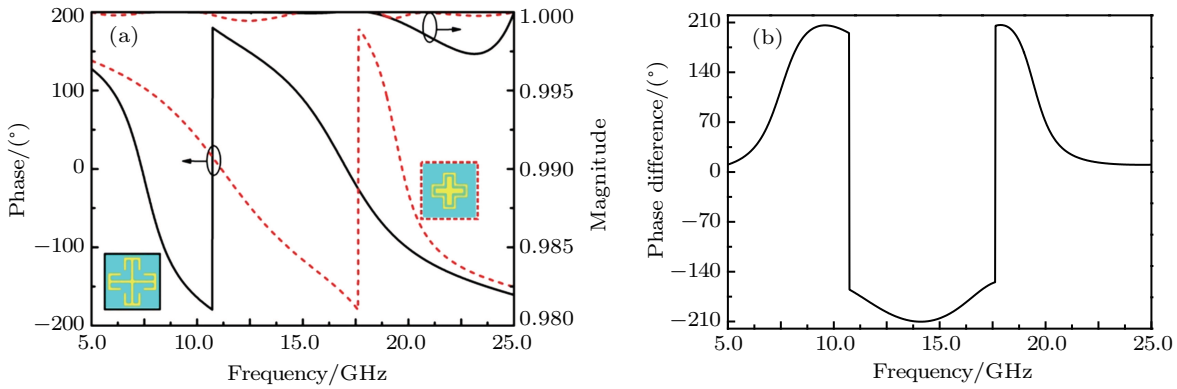


Fig. 5. (color online) (a) Reflection coefficients and (b) phase difference of both AMCs as a function of frequency.

Figure 5(a) depicts the reflection coefficients of both AMCs as a function of frequency. As can be seen, AMC-1 exhibits 0° phase reflection at 11.1 GHz and 19.7 GHz, whereas the 0° phase reflection of AMC-2 occurs at 7.4 GHz and 17.1 GHz. They both have two magnetic resonances. Moreover, it is learned that the inversion point of AMC-2 in the reflection phase curve is at the first resonance of AMC-1, and that of AMC-1 is in proximity to the second resonance of AMC-2. This is very essential to guarantee the destructive interference condition over an ultrawide band. As a consequence, the phase difference shown in Fig. 5(b) fluctuates around 180° in a broad frequency band. The bandwidth characterized by ±30° tolerance is observed from 7.9 GHz to 19.2 GHz, corresponding to a fractional bandwidth of 83.4%. Within this band, the metasurface by combining these AMC unit cells in a novel chessboard configuration is expected to have a desirable backscatter RCS reduction level. To have an intuitive understanding of the dual-resonance of the proposed AMC structures, the electric field distributions on the top layer are simulated at the corresponding resonant frequencies, as shown in Fig. 6. It can be clearly seen that the inner cross structure and the outer cross loop structure contribute to two resonances of AMC-1, respectively. Similarly, the resonances of different parts of AMC-2 result in a dual-resonance characteristic.

Given the structures of the two AMCs, the entire metasurface structure with aid of the CST microwave studio is readily constructed. Figure 7(a) depicts the layout for one tile of a novel chessboard metasurface (NCM). For comparison, the configuration with 2×2 tiles of a conventional chessboard metasurface (CCM) is also afforded, see Fig. 7(b). As can be seen, the novel configured metasurface is constructed by four triangular-type subsegments instead of the conventional square-type counterparts. Each subsegment is filled

with AMC-1 or AMC-2 of identical geometrical parameters and the adjacent subsegments are configured alternately with AMC-1 and AMC-2. As a consequence, the horizontal or vertical interface formed between adjacent subsegments is replaced by the diagonal or off-diagonal counterpart, which is the key factor for a scattering pattern with more lobes. Because the RCS reduction performance can be determined analytically in terms of tile spacing, we use a subgroup of 6×6 identical elements as a tile to achieve excellent RCS reduction performance.

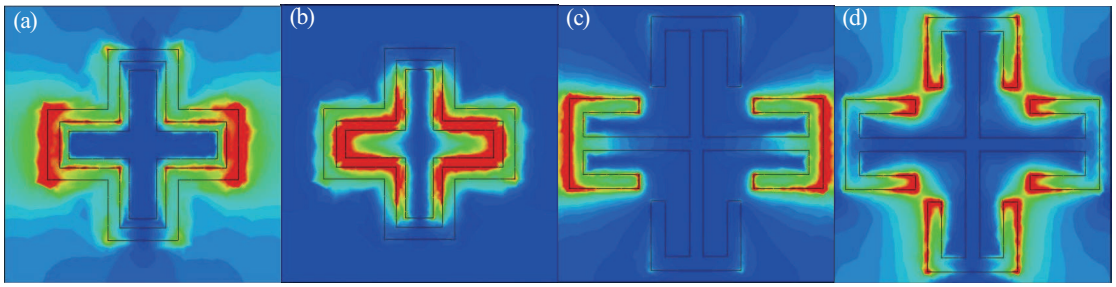


Fig. 6. (color online) Electric field distributions of (a) AMC-1@11.1 GHz , (b) AMC-1@19.7 GHz; (c) AMC-2@7.4 GHz, and (d) AMC-2@17.1 GHz for *x*-polarized incident.

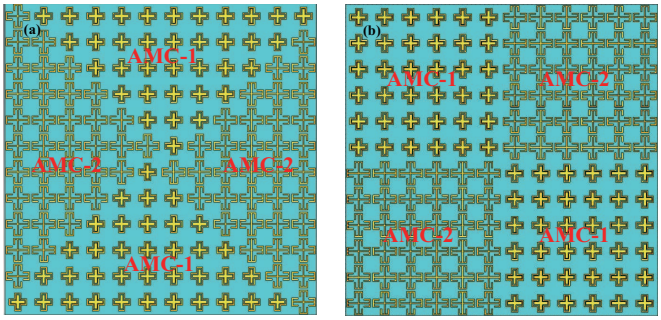


Fig. 7. (color online) Layouts of (a) one tile of NCM and (b) 2×2 tiles of CCM.

3. Numerical and experimental results

3.1. Numerical results

For fair comparison, both metasurfaces with the same total dimension of 288 mm×288 mm are simulated in CST microwave studio. The monostatic RCS reduction versus frequency under normal incidence for both metasurfaces are presented in Fig. 8. The values are normalized to the peak scattered intensity of an equal-sized PEC plate to show their ability for RCS reduction. Due to the dual-mode characteristic of the AMC unit cells, the RCS shown in Fig. 8 is reduced by more than 10 dB within the frequency band of 8.2–17.4 GHz for the NCM, and the maximum RCS reduction of more than 25 dB is obtained at 13.3 GHz. Thus, the simulated RCS reduction bandwidth is 71.9%. For the CCM, we do not expect such ultra-wideband RCS reduction performance due to undesired high values between 9.4 GHz and 10.4 GHz. The discrepancy between the simulated operational bandwidth and the predicted bandwidth (7.9–19.2 GHz) is mainly attributed to the edge effects and high-order modes at high frequencies. Table 1 compares the bandwidth between the NCM and previous work. It is clearly seen that our NCM exhibits a broader bandwidth compared with the other broadband low scattering metasurface.

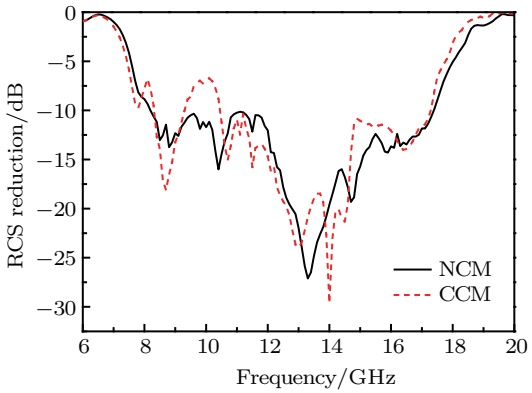


Fig. 8. (color online) Comparison of monostatic RCS reduction performance under normal incidence between two configurations.

Table 1. Comparison of bandwidth between NCM and previous work.

Reference	Frequency range (< −10 dB)/GHz	Bandwidth/%
[5]	7–13	60
[7]	8–12	40
[11]	9–15	50
[12]	4.1–7.9	63
Our work	8.2–17.4	71.9

Moreover, the simulation results of scattered field intensity at 13.3 GHz for both metasurfaces are presented in Fig. 9. As expected, the backscatter is significantly reduced due to the phase cancellation of the reflected fields from the two AMC structures. The simulation results are in good agreement with the theoretical prediction shown in Fig. 3. It can be observed from Fig. 9 that there are eight main scattered lobes for the NCM, while only four main lobes for the CCM. The scattered field along the $\varphi = 0^\circ$ plane and along the plane with the maximum bistatic RCS are given in Fig. 10 for a quantitative comparison. The RCS for both metasurfaces are compared with

the RCS for the equal-sized PEC plate. In the $\varphi = 0°$ plane, the maximum RCS for the CCM is -9.6 dB at $\theta = -39°$, which is 19.85 dB less than the maximum RCS for the PEC plate, and the maximum RCS is -13.2 dB at $\theta = -39°$ for the NCM, being 23.45 dB below the peak RCS of the PEC plate. The maximum bistatic RCS occurs at the $\varphi = 45°$ plane and the $\varphi = 17°$ plane for CCM and NCM, respectively. Figure 10(b) shows that the scattered power is mainly redirected to $\theta = \pm 24°$ for the CCM and to $\theta = \pm 28°$ for the NCM. The maximum bistatic RCS of the PEC plate, the CCM, and the NCM is 10.25 dB, 2.99 dB, and -0.30 dB, respectively. Consequently, the maximum RCS of NCM is reduced by more than 3 dB with respect to that of CCM.

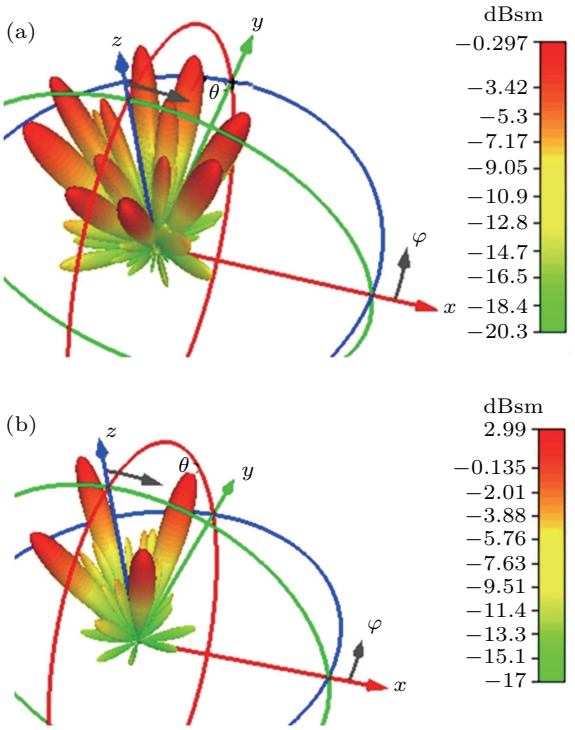


Fig. 9. (color online) The simulated 3D plots of scattered field intensities for (a) NCM and (b) CCM.

As is known, the phase behavior of AMC structure depends on the incident angle of incoming waves. Therefore, the operational bandwidth for RCS reduction will also be affected by the incident angle. To examine such an effect, we depict in Fig. 11 the phase response and RCS reduction of the metasurface as a function of frequency for different incident angles. It is found that the phase difference undergoes slight fluctuations as the incident angle increases and thus deviates from $\pm 180°$ with a tolerance of $\pm 40°$. Such phase tolerance is within an acceptable level for device functionality. Table 2 summarizes the operational 6 dB RCS reduction bandwidth for each incidence angle. From Table 2, we can see that the bandwidth decreases a little as the incident angle grows. However, low reflection properties are still kept over a wide frequency range for the proposed metasurface.

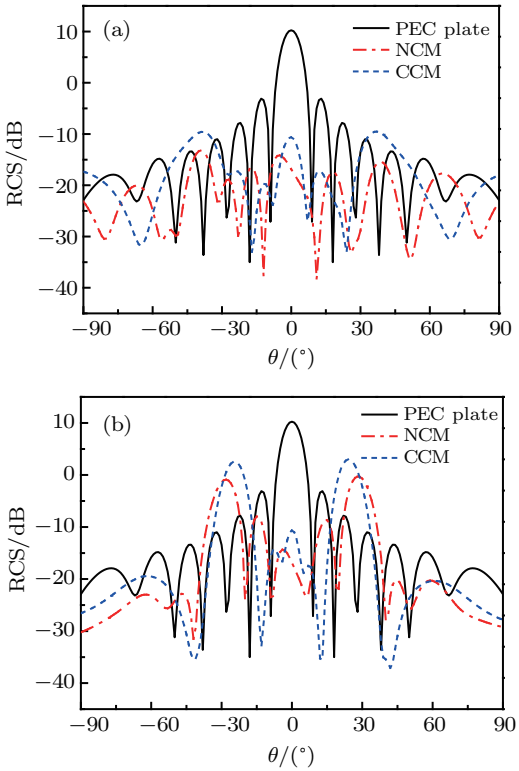


Fig. 10. (color online) Simulated bistatic RCS of (a) $\varphi = 0°$ plane and (b) φ plane with the maximum bistatic RCS (45° for CCM and 17° for NCM) at 13.3 GHz.

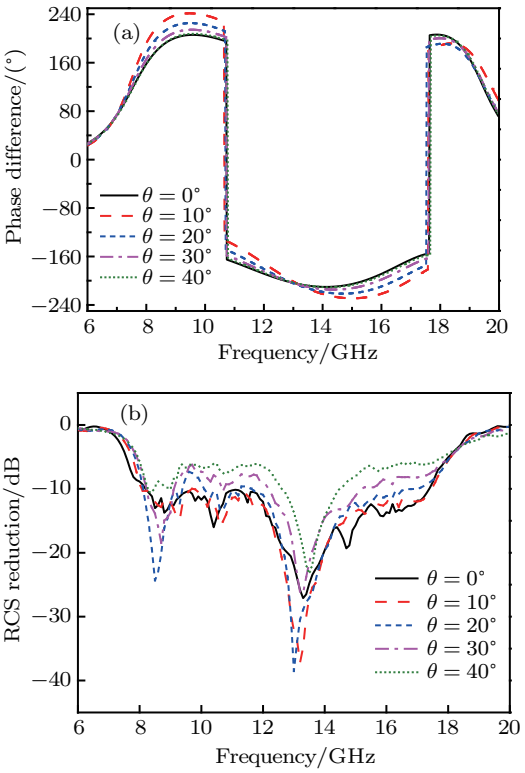


Fig. 11. (color online) (a) Phase difference and (b) monostatic RCS reduction versus frequency for different incident angles.

Table 2. Operational 6 dB RCS reduction bandwidth as a function of the incidence angle.

Incident angle/(°)	Bandwidth/%
0	79.7
10	77.5
20	76.4
30	76.0
40	72.9

3.2. Fabrication and measurements

To experimentally demonstrate the proposed ultra-wideband low-reflection properties, an NCM sample occupying an area of 288 mm×288 mm (4×4 tiles) was fabricated using standard printed circuit board (PCB) technology, see Fig. 12(a). Due to limited experimental resources available for bistatic RCS measurement, only monostatic RCS under normal incidence measurement was carried out in an anechoic chamber. In the experimental setup illustrated in Fig. 12(b), two identical wideband ridged horn antennas operating from 2 GHz to 18 GHz were used as the transmitting and receiving antennas which are connected to two ports of a vector network analyzer. A wideband amplifier operating from 6 GHz to 18 GHz was also used to boost the transmitted power. The measured sample was placed 3 m from the horns to ensure the plane wave illumination. The height of the sample was kept the same as that of the horns.

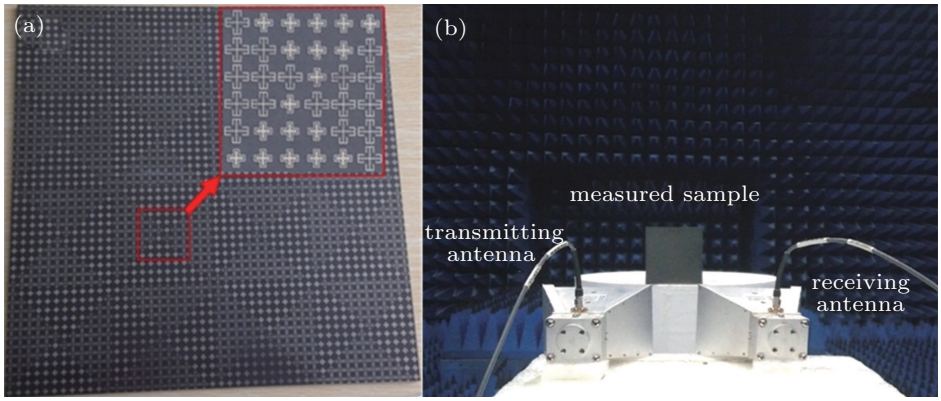


Fig. 12. (color online) (a) Photograph of the fabricated sample and (b) experimental setup.

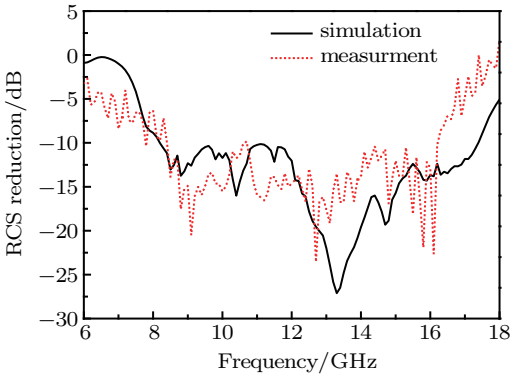


Fig. 13. (color online) Comparison of simulated and measured monostatic RCS reduction.

The backscatter has been evaluated by reflection coefficient characterization of the horn antenna. The backscatter from an equal-sized PEC plate was also measured to characterize the RCS reduction performance. Figure 13 compares the simulated and measured monostatic RCS reduction performance. A reasonable agreement of results is inspected in the entire observed band. The slight discrepancies at high frequencies are induced by the tolerances that are inherent in the fabrication process and partially to the misalignment of horn and metasurface in measurements. As such, the phase difference under two orthogonal polarizations deviates from the model in numerical calculations. Nevertheless, the measured RCS has been reduced by more than 10 dB from 8.4 GHz to 16.3 GHz.

4. Conclusion

A novel ultra-wideband metasurface for RCS reduction is designed, fabricated, and measured. The proposal is conceptually validated first by theoretically evaluating the scattered fields of different configurations through array theory. Two dual-mode AMC structures are designed cautiously to obtain $180^\circ \pm 30^\circ$ phase difference over a wide frequency range. The proposed triangle-type AMC structure generates eight scattered main lobes and a null in the special direction. A good agreement of results is observed between simulations and measurements, showing over 70% operational bandwidth for 10 dB RCS reduction.

References

[1] Fante R L and McCormack M T 1988 *IEEE Trans. Antennas Propag.* **36** 1443

[2] Costa F, Monorchio A and Manara G 2010 *IEEE Trans. Antennas Propag.* **58** 1551

[3] Xu H X, Wang G M, Qi M Q, Liang J G, Gong J Q and Xu Z M 2012 *Phys. Rev. B* **86** 205104

[4] Shen X P, Yang Y, Zang Y Z, Gu J, Han J G, Zhang W L and Cui T J 2012 *Appl. Phys. Lett.* **101** 154102

[5] Wang K, Zhao J, Cheng Q, Dong D S and Cui T J 2014 *Sci. Rep.* **4** 5935

[6] Yan X, Liang L J, Yang J, Liu W W, Ding X, Xu D G, Zhang Y T, Cui T J and Yao J Q 2015 *Opt. Express* **23** 29128

[7] Xie S Y, Huang J J, Liu L G and Yuan N C 2014 *Chin. Phys. B* **23** 047802

[8] Li Y F, Zhang J Q, Qu S B, Wang J F, Chen H Y, Xu Z and Zhang A X 2014 *Appl. Phys. Lett.* **104** 221110

[9] Wu C J, Cheng Y Z, Wang W Y, He B and Gong R Z 2015 *Acta Phys. Sin.* **64** 164102 (in Chinese)

[10] Paquay M, Iriate J C, Ederra I, Gonzalo R and Maagt P D 2007 *IEEE Trans. Antennas Propag.* **55** 3630

[11] Edalati A and Sarabandi K 2014 *IEEE Trans. Antennas Propag.* **62** 747

[12] Chen W G, Balanis C A and Birtcher C R 2015 *IEEE Trans. Antennas Propag.* **63** 2636

[13] Zheng Y J, Gao J, Cao X Y, Li S J, Yang H H, Li W Q, Zhao Y and Liu H X 2015 *Acta Phys. Sin.* **64** 024219 (in Chinese)

[14] Pan W B, Huang C, Pu M B, Ma X L, Cui J H, Zhao B and Luo X G 2016 *Sci. Rep.* **6** 21462

[15] Sievenpiper D, Zhang L J, Broas R F J, Alexópolous N G and Yablonovitch E 1999 *IEEE Trans. Microw. Theory Tech.* **47** 2059